

1 **Use of *in situ* and airborne multiangle data to assess**
2 **MODIS- and Landsat-based estimates of surface albedo**

3
4
5 Miguel O. Román^{a,*}, Charles K. Gatebe^{a,b}, Yanmin Shuai^{a,c},
6 Zhuosen Wang^{d,e}, Feng Gao^f, Jeff Masek^a, and Crystal B. Schaaf^g

7
8 ^a*NASA Goddard Space Flight Center, Greenbelt, Maryland, USA*

9 ^b*Universities Space Research Association (USRA), Columbia, Maryland, USA*

10 ^c*Earth Resources Technology Inc., Laurel, Maryland, USA*

11 ^d*Center for Remote Sensing, Department of Geography and Environment, Boston University, Boston, MA, USA*

12 ^e*State Key Laboratory of Remote Sensing Science, Center for Remote Sensing and GIS of Geography College,*

13 *Beijing Key Laboratory for Remote Sensing of Environment and Digital Cities, Beijing Normal University, Beijing, China*

14 ^f*USDA-ARS Hydrology and Remote Sensing Laboratory, Beltsville, Maryland, USA*

15 ^g*EEOS Department, University of Massachusetts Boston, Boston, Massachusetts, USA*

16
17

18

19

20 * Corresponding author. Tel.: +1 301 614 5498; fax: +1 301 614 5269

21 E-mail address: Miguel.O.Roman@nasa.gov

22

23 **Abstract –**

24 The quantification of uncertainty of global surface albedo data and products is a critical part
25 of producing complete, physically consistent, and decadal land property data records for studying
26 ecosystem change. A current challenge in validating satellite retrievals of surface albedo is the
27 ability to overcome the spatial scaling errors that can contribute on the order of 20% disagree-
28 ment between satellite and field-measured values. Here, we present the results from an uncertain-
29 ty analysis of MODerate Resolution Imaging Spectroradiometer (MODIS) and Landsat albedo
30 retrievals, based on collocated comparisons with tower and airborne multiangular measurements
31 collected at the Atmospheric Radiation Measurement Program's (ARM) Cloud and Radiation
32 Testbed (CART) site during the 2007 Cloud and Land Surface Interaction Campaign (CLAS-
33 IC'07). Using standard error propagation techniques, airborne measurements obtained by
34 NASA's Cloud Absorption Radiometer (CAR) were used to quantify the uncertainties associated
35 with MODIS and Landsat albedos across a broad range of mixed vegetation and structural types.
36 Initial focus was on evaluating inter-sensor consistency through assessments of temporal stabili-
37 ty, as well as examining the overall performance of satellite-derived albedos obtained at all diur-
38 nal solar zenith angles. In general, the accuracy of the MODIS and Landsat albedos remained
39 under a 10% margin of error in the SW (0.3 - 5.0 μm) domain. However, results reveal a high
40 degree of variability in the RMSE (root mean square error) and bias of albedos in both the visible
41 (0.3 - 0.7 μm) and near-infrared (0.3 - 5.0 μm) broadband channels; where, in some cases, re-
42 trieval uncertainties were found to be in excess of 20%. For the period of CLASIC'07, the prima-
43 ry factors that contributed to uncertainties in the satellite-derived albedo values include: (1) the
44 assumption of temporal stability in the retrieval of 500 m MODIS BRDF values over extended

45 periods of cloud-contaminated observations; and (2) the assumption of spatial and structural un-
46 iformity at the Landsat (30 m) pixel scale.

47 **1. Background**

48 A major goal of international Earth observation efforts is the long term monitoring of terre-
49 trial essential climate variables and the production of consistent land surface radiation parame-
50 ters for rigorous modeling studies. With the advent of a new generation of multi-sensor data and
51 products for Land science applications, recent efforts have explored the “MODISization” of na-
52 dir-looking satellite sensors to obtain high-resolution (30 m) MODIS-driven land surface para-
53 meters (Gao et al. 2006; Roy et al. 2008). For example, (Shuai et al. 2011) combined both Land-
54 sat reflectance (Masek et al. 2006) and high quality 500 m MODIS BRDF (Bidirectional Reflec-
55 tance Distribution Function) parameters (Lucht et al. 2000; Schaaf et al. 2002; Schaaf et al.
56 2008) to retrieve 30 m resolution estimates of surface albedo. By capturing seasonal trends at the
57 characteristic scale of vegetation change (~1 ha), these approaches have the potential to improve
58 our understanding of the climate consequences of global land cover change and ecosystem dis-
59 turbance (Barnes and Roy 2008; Masek et al. 2008). .

60 The quantification of uncertainty of global surface albedo data and products from both
61 MODIS and Landsat satellites is a critical part of producing complete, physically consistent,
62 global, and decadal land property data records. The MODIS BRDF/albedo standard product,
63 available globally since 2000 at resolutions from 0.5 to 5 km, has been validated to Committee
64 on Earth Observation Satellites (CEOS) Stage 2 (i.e., over a widely distributed set of locations
65 and time periods via several ground-truth and validation efforts). This validation stage is a pre-

66 requisite for any data product that is used for monitoring change over time (Morisette et al.
67 2002). The high-quality primary algorithm for the MODIS standard albedo product (MCD43)
68 has also been shown to produce consistent global quantities over a variety of land surface types
69 and snow-covered conditions (Jin et al. 2003a; Jin et al. 2003b; Salomon et al. 2006; Liu et al.
70 2009; Román et al. 2009; Román et al. 2010; Wang et al. 2011). On the other hand, the combined
71 MODIS/Landsat albedo product (hereby termed ‘Landsat albedo’), which is based on per-class
72 MODIS BRDF shapes based on uniform land cover characteristics, has been shown to provide a
73 more detailed landscape texture and achieve good agreement with in-situ data over a limited
74 number of field stations (Shuai et al. 2011). Additional assessments over a wide range of spatial
75 (from 10s of meters to 5-30 km) and temporal scales (from daily to monthly) are nonetheless re-
76 quired to accurately provide end users with a pixel-specific measure of product uncertainty –
77 both in terms of retrieval quality (e.g. given a limited number of cloud-free satellite observations)
78 and their ability to capture albedo trends under conditions of seasonal and/or rapid surface
79 change.

80 A current challenge in validating satellite albedo retrievals is the ability to overcome the spa-
81 tial scaling errors that contribute disagreement between satellite and field-measured values,
82 which can be on the order of 20% (Jin et al. 2003b; Salomon et al. 2006; Liu et al. 2009; Román
83 et al. 2010). Recent studies have acquired measurements atop tall (> 400 m) towers to properly
84 “scale-up” to satellite measurements (Augustine et al. 2005; Román et al. 2009). Other efforts
85 have used high resolution imagery to consider the spatial representativeness of the tower obser-
86 vation footprint to the MODIS pixel (Susaki et al. 2007; Román et al. 2009). While these me-
87 thods provide a good means by which direct “point-to-pixel” assessments can be performed with

88 high confidence; they present their own set challenges (e.g., in the United States, instruments
89 atop tall towers cannot be left operating year-round, due to heavy icing and bad weather). On ac-
90 count of the uncertainties arising from direct comparison between sparsely sampled *in situ* mea-
91 surements and their corresponding satellite products, a formal assessment has yet to be carried
92 out to characterize the ability of the MODIS and Landsat data to capture diurnal trends in albedo
93 across spatially heterogeneous environments. To address these issues, we present the results from
94 an uncertainty quantification of MODIS and Landsat albedo retrievals based on collocated com-
95 parisons with tower and airborne measurements. For the airborne datasets, we have employed the
96 retrieval scheme presented in Román et al. (2011a), which follows the operational sequence used
97 to retrieve the MODIS surface reflectance and BRDF/albedo products, based on high-quality
98 multiangular reflectance measurements obtained by NASA's Cloud Absorption Radiometer
99 (CAR) (King et al. 1986; Gatebe et al. 2003). This study focuses on CAR retrievals obtained
100 over the Atmospheric Radiation Measurement Program's (ARM) Cloud and Radiation Testbed
101 (CART) site during the 2007 Cloud and Land Surface Interaction Campaign (CLASIC'07) (Bin-
102 dlish et al. 2009; Heathman et al. 2009).

103 **2. Albedo retrieval strategy**

104 In this section, we briefly review the albedo retrieval methods used by the MODIS, Landsat,
105 and CAR instruments, and assess the calibration performance of the CAR spectral channels dur-
106 ing the period of CLASIC'07. Readers are referred to Sections 2 and 3 in Román et al. (2011a)
107 for detailed descriptions of the CLASIC'07 experiment (including retrieval of CAR and MODIS

108 BRDF/albedo datasets); and Section 2 in Shuai et al. (2011) for a complete description of the
 109 Landsat albedo retrieval strategy.

110 **2.1 Instantaneous albedos from CAR, MODIS, and Landsat**

111 The CAR, MODIS, and Landsat albedo retrieval schemes employ the BRDF kernel model
 112 parameters from the reciprocal version of the semiempirical RossThick-LiSparse model
 113 (RTLSR) (Wanner et al. 1995; 1997; Lucht et al. 2000):

114 $R_{\Lambda}(\Omega_v, \Omega_s) = f_{iso,\Lambda} + f_{vol,\Lambda} K_{vol}(\Omega_v, \Omega_s) + f_{geo,\Lambda} K_{geo}(\Omega_v, \Omega_s)$ (1)

115 Here, Ω_v and Ω_s are the viewing and solar geometries, which are each defined by zenith and azi-
 116 muthal angles (θ, ϕ). K_{vol} is the coefficient for the RossThick volume scattering kernel (Ross
 117 1981); K_{geo} is the coefficient of the LiSparse-Reciprocal geometric scattering kernel (Li and
 118 Strahler 1992); and $f_{x,\Lambda}$ are the RTLSR kernel weights x in waveband Λ with limits $[\Lambda_{min}, \Lambda_{max}]$
 119 (Wanner et al. 1995; Lucht et al. 2000). The RTLSR kernel weights are then used to compute in-
 120 trinsic surface albedos (i.e., black sky albedo for direct beam at local solar noon and white sky
 121 albedo for isotropic diffuse radiation) (Martonchik et al. 2000; Schaepman-Strub et al. 2006):

122
$$\begin{aligned} \bar{R}_{\Lambda}(\Omega_i) &= \frac{1}{\pi} \int_0^{2\pi} d\phi_v \int_0^1 R_{\Lambda}(\Omega_v, \Omega_i) \mu_v d\mu_v \\ &= f_{iso\Lambda} + f_{vol\Lambda} \bar{K}_{vol\Lambda}(\Omega_s) + f_{geo\Lambda} \bar{K}_{geo\Lambda}(\Omega_s) \end{aligned} \quad (2)$$

123
$$\begin{aligned} \bar{\bar{R}}_{\Lambda} &= \frac{1}{\pi} \int_0^{2\pi} d\phi_i \int_0^1 \bar{R}_{\Lambda}(\Omega_i) \mu_i d\mu_i \\ &= f_{iso\Lambda} + f_{vol\Lambda} \bar{\bar{K}}_{vol\Lambda} + f_{geo\Lambda} \bar{\bar{K}}_{geo\Lambda} \end{aligned} \quad (3)$$

125 where, $R_\Lambda(\Omega_v, \Omega_i) = \pi BRDF_\Lambda$ (unitless), is the ratio of the surface BRDF to that of a perfect
 126 Lambertian reflector, which can be approximated by measurement over some (small) finite angle
 127 with diffuse illumination and multiple interaction effects accounted for or assumed zero (Lyapus-
 128 tin and Privette 1999). Subscripts v and i denote the upper ‘viewing’ and ‘incident’ hemispheres.

129 $\bar{R}_\Lambda(\Omega_s)$ is the black-sky albedo, $\bar{\bar{R}}_\Lambda$ is white-sky albedo, $\bar{K}_{vol}(\Omega_v)$ and $\bar{K}_{geo}(\Omega_v)$ are the direc-
 130 tional-hemispherical integrals, and $\bar{\bar{K}}_{vol}(\Omega_v)$ and $\bar{\bar{K}}_{geo}(\Omega_v)$ are the bihemispherical integrals of
 131 K_{vol} and K_{geo} . Other terms in Eq. (2) and (3) are:

$$132 \quad \mu_y = \cos(\vartheta_y); \quad y = v \text{ or } i \quad (4)$$

133 To accurately compare these intrinsic quantities against ground-based albedos, the black-sky and
 134 white-sky albedos must be combined as a function of solar geometry and atmospheric state to
 135 compute instantaneous albedo under assumptions of isotropic diffuse illumination:

$$136 \quad A_{\Lambda Iso}(\Omega_s) = \frac{f_{iso\Lambda} + (1 - D_{0\Lambda}) \left[f_{vol\Lambda} \bar{K}_{vol}(\Omega_s) + f_{geo\Lambda} \bar{K}_{geo}(\Omega_s) \right] +}{D_{0\Lambda} \left[f_{vol\Lambda} \bar{\bar{K}}_{vol}(\Omega_s) + f_{geo\Lambda} \bar{\bar{K}}_{geo}(\Omega_s) \right]} \quad (5)$$

137 where $D_{0\Lambda}$ (unitless) is the proportion of diffuse illumination for an absorbing lower boundary
 138 (Lewis and Barnsley 1994; Lucht et al. 2000). The MODIS BRDF shape derived from clear-sky
 139 observations can then be used to derive albedo values in all sky conditions (Liu et al. 2009).
 140 Most recently, the computation of MODIS instantaneous albedos was updated to account for the
 141 effects of multiple scattering and anisotropic diffuse illumination (Román et al. 2010):

142 $A_{\Lambda}(\Omega_s) \approx f_{iso\Lambda} + f_{vol\Lambda} \overline{\overline{K''}}_{vol\Lambda}(\Omega_s) + f_{geo\Lambda} \overline{\overline{K''}}_{geo\Lambda}(\Omega_s)$ (6)

143 $\overline{\overline{K''}}_{x\Lambda}(\Omega_s) = (1 - D_{0\Lambda}) \overline{K}_x(\Omega_s) + D_{0\Lambda} \overline{\overline{K'}}_{x\Lambda}$ (7)

144 $\overline{\overline{K'}}_{x\Lambda} = \frac{1}{\pi} \int_0^{2\pi} d\phi_i \int_0^1 \overline{K}_x(\Omega_i) N_{sky\Lambda}(\Omega_i) \mu_i d\mu_i$ (8)

145 $\overline{K}_x(\Omega_v) = \frac{1}{\pi} \int_0^{2\pi} d\phi_i \int_0^1 K_x(\Omega_v, \Omega_i) \mu_i d\mu_i$ (9)

146 where, $N_{sky\lambda}(\Omega_i)$ is the normalized sky radiance distribution under an absorbing lower boundary

147 and $\overline{\overline{K'}}_{x\Lambda}$ is the $N_{sky\lambda}$ -weighted bihemispherical integral of $K_x(\Omega_v, \Omega_s)$ (where $x = vol$ or geo).

148 Intrinsic albedo quantities derived from RTLSR BRDF model inversions can then be combined
 149 with in-situ estimates of cloud fraction (< 0.6), 550 nm aerosol optical depth (AOD), solar zenith
 150 angle (SZA), and $D_{0\Lambda}$ to compute clear-sky instantaneous albedos from MODIS, Landsat, and
 151 CAR data.

152 The kernel-driven models employed by the MODIS and Landsat albedo products are also
 153 identified as part of the heritage algorithms used to generate the Visible Infrared Imager Radi-
 154 ometer Suite's (VIIRS) Land Environmental Data Records (EDRs); which aim to ensure continu-
 155 ity for AVHRR and MODIS observations by providing high temporal resolution and wide area
 156 coverage (Lee et al. 2010). The VIIRS Land EDRs are currently being evaluated by NASA and
 157 NOAA to assess their suitability for operational weather forecasting and long-term climate moni-
 158 toring applications (Román et al. 2011b).

159 **2.2 Narrowband to Broadband Conversion**

160 Since field-measured albedos are commonly measured as broadband quantities, an equiva-
 161 lent set of broadband albedos for MODIS and Landsat were generated for the UV-Visible (0.3 -
 162 0.7 μm), NIR (0.7 - 5.0 μm), and the entire spectrum of solar radiation ([SW] 0.3 - 5.0 μm),
 163 based on empirical relations between ground-based albedo measurements and satellite observa-
 164 tions – *cf.*, Eqs. (11) and (15) in Liang (2001). Broadband albedos were also derived for CAR
 165 measurements by calculating the ratio of broadband upwelling radiative flux to broadband
 166 downwelling flux (Liang 2001; Liang et al. 2003):

$$167 F(\Omega_s) = \frac{\int_{\Lambda_{\min}}^{\Lambda_{\max}} A(\Omega_s) D(\Omega_s, \Lambda) d\Lambda}{\int_{\Lambda_{\min}}^{\Lambda_{\max}} D(\Omega_s, \Lambda) d\Lambda} = \sum_i c_i A(\Omega_s, \Lambda_i) \quad (10)$$

168 Then, CAR narrowband-to-broadband spectral albedo coefficients, c_i , were generated for each
 169 spectral band by determining the downward fluxes (i.e. direct and diffuse) using a library of 30
 170 reflectance spectra of representative land covers in the ARM Southern Great Plains (SGP) region
 171 (Trishenko et al. 2003):

$$172 A_{short} = 0.160\alpha_1 + 0.291\alpha_2 + 0.243\alpha_3 + 0.116\alpha_4 + 0.112\alpha_5 + 0.081\alpha_7 - 0.0015 \quad (11)$$

$$173 A_{NIR} = 0.039\alpha_1 + 0.504\alpha_2 - 0.071\alpha_3 + 0.105\alpha_4 + 0.252\alpha_5 + 0.069\alpha_6 + 0.101\alpha_7 \quad (12)$$

$$174 A_{visible} = 0.331\alpha_1 + 0.424\alpha_3 + 0.246\alpha_4 \quad (13)$$

175 The upward fluxes were directly obtained from the library of 30 SGP reflectance spectra; while
176 the downward fluxes were obtained by performing multiple MODTRAN®5.1 (Berk et al. 2004)
177 runs for a broad range of snow-free conditions (i.e., 21 atmospheric visibility values for different
178 aerosol loadings, 2 atmospheric profiles, and solar zenith angles ranging from 0° - 80° with the
179 increment of 1°).

180 **2.3 CAR instrument performance during CLASIC'07**

181 During the CLASIC'07 experiment, radiometric calibration of the CAR spectral channels
182 was made at the NASA Goddard Space Flight Center Radiometric Calibration Facility (GSFC-
183 RCF) (Butler and Barnes 2003). A description of the calibration scheme, using a series of inte-
184 grating spheres with diameters of 1.83 m, 1.22 m, and 0.51 m, covering all of the CAR's spectral
185 channels, can be found in Gatebe et al. (2007). The conversion from Digital Numbers (DNs) to
186 Level 1 at-sensor radiances is determined from the instrument's response for at least two known
187 radiance levels and then determining the instrument gain (slope) and offset (intercept) for each
188 wavelength across the sensor band pass. The estimated errors associated with this radiometric
189 conversion vary from $\pm 1\%$ to $\pm 3\%$ for all spectral channels (Gatebe et al. 2003; Gatebe et al.
190 2007). Radiometric calibration was performed prior to and after CLASIC'07. In the past, to de-
191 termine a suitable calibration for a given flight during the experiment, a linear change between
192 the preflight and postflight calibration was assumed as a function of only the number of flights
193 flown during an entire campaign. For the CLASIC'07 experiment, however, both the pre- and
194 post-calibration coefficients were averaged. This was found to be representative of each flight
195 scenario, and made it easier to account for uncertainties related to calibration, stability, and wa-

196 velength errors. We note that the calibration ratios, postflight-to-preflight, varied between 0.9691
197 (at $\Lambda = 0.472 \mu\text{m}$) and 1.1845 (at $\Lambda = 0.340 \mu\text{m}$).

198 **Table 1. Remotely-sensed albedo retrieval scenarios obtained during CLASIC'07 for MODIS,**
199 **Landsat, CAR in medium resolution mode (MRM), and CAR in coarse resolution mode (CRM).**

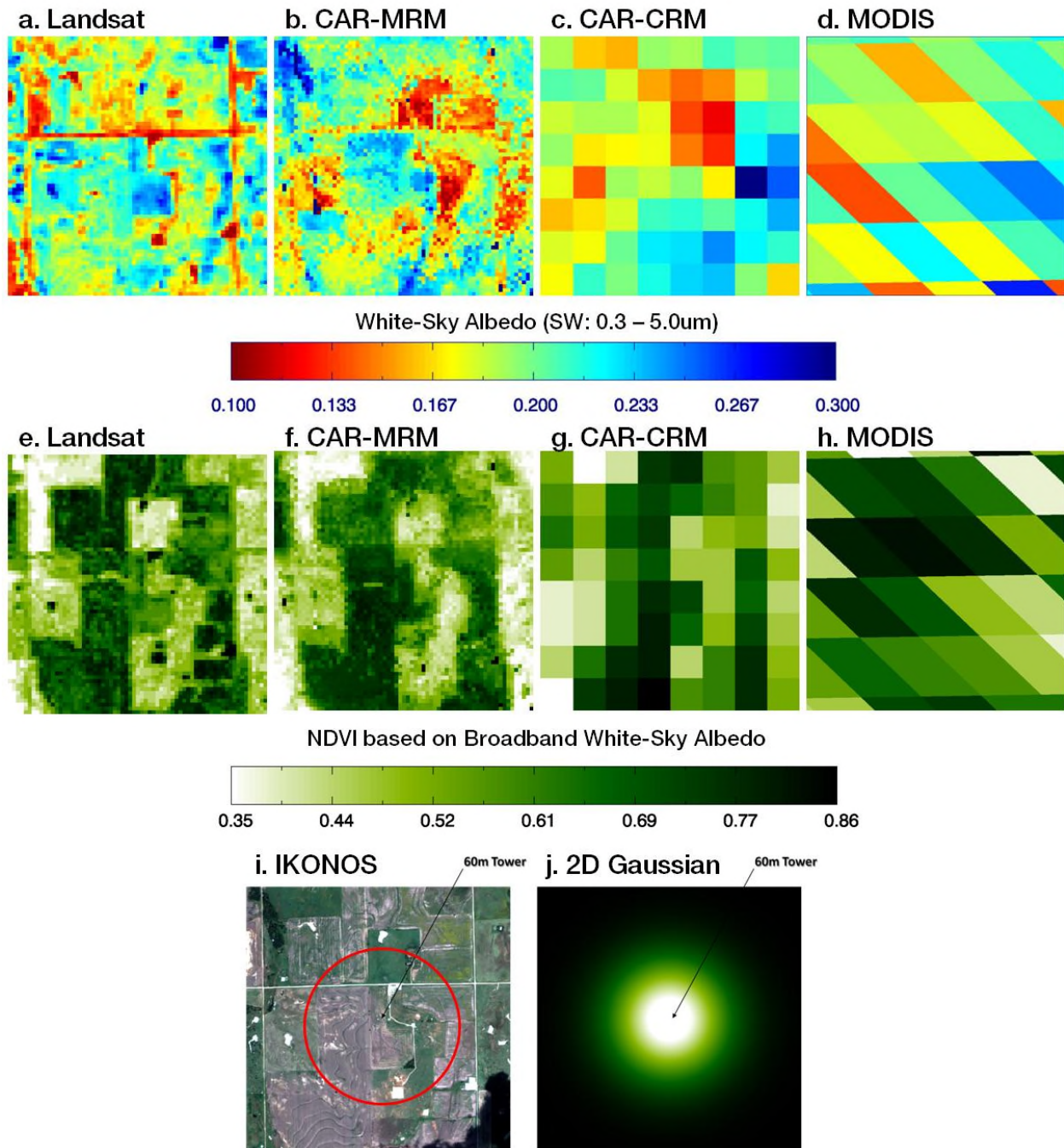
| Instrument | GIFOV (m) | Scale (m) | BRDF Retrieval Period (DOY) | Albedo Reconstruction Period (DOY) |
|------------------|------------|-----------|-----------------------------|------------------------------------|
| MODIS Terra/Aqua | 436 – 1686 | 500 | 145-193 | 153-155; 159-190 |
| Landsat TM | 30 | 30 | 153-168 | 153-155 |
| CAR-MRM | 15 – 45 | 30 | 175 | 153-155 |
| CAR-CRM | 90 - 360 | 250 | 175 | 159-190 |

200

201 **3. Retrieval scenarios during CLASIC'07**

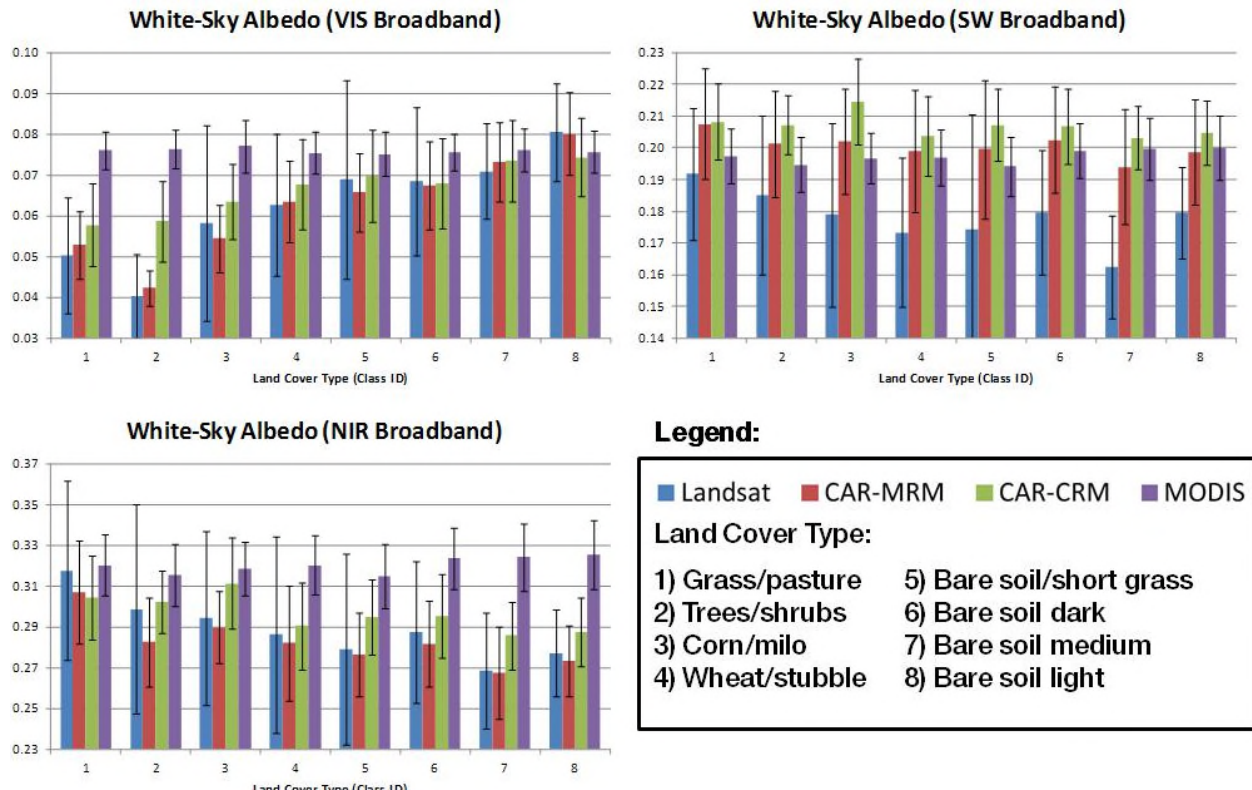
202 Table 1 provides a summary of the individual BRDF retrieval and albedo reconstruction pe-
203 riods for CAR, MODIS, and Landsat. Note that the retrieval scenarios varied by sensor. For in-
204 stance, Landsat albedos were reconstructed for a short time period (Day of the year, DOY 153-
205 155) to better represent the per-class albedo-to-nadir-reflectance (A/N) ratios derived from the
206 concurrent MODIS acquisition period. Conversely, the CAR albedos are based on two different
207 modes: a Medium Resolution Mode (CAR-MRM) to match the scale of Landsat data; and a
208 Coarse Resolution Mode (CAR-CRM) to match the scale of MODIS data (*cf.*, Fig. 9 in Román et
209 al. 2011a). The CAR measurements are based on CLASIC Flight #1928 (DOY 175, 2007). Ac-
210 cordingly, a longer measurement period was also examined (i.e., DOY 159-190) to evaluate the
211 ability of the CAR and MODIS data to represent the landscape conditions surrounding the entire
212 CLASIC'07 period.

213



214

215 **Fig. 1.** (a. – h.) 2 km x 2 km subsets illustrating retrievals of white-sky albedo (WSA) and
 216 broadband NDVI. The Broadband NDVI values are based on the UV-VIS and NIR portions of the solar
 217 spectrum: $NDVI = (WSA_{NIR} - WSA_{VIS}) / (WSA_{NIR} + WSA_{VIS})$. (i.) IKONOS true-color scene,
 218 retrieved on 1 July 2007, denotes the ~960 m ground footprint as seen by the downward-facing pyra-
 219 nometer atop the CART site's 60 m radiation tower. (j.) Spatially-integrated albedos for CAR,
 220 Landsat, and MODIS, were computed based on a 2D Gaussian filter representing the tower foot-
 221 print.



222
223 **Fig. 2. Comparisons of intrinsic white-sky albedos derived from Landsat, CAR, and MODIS data**
224 **shown for individual land cover types present across the ARM CART during CLASIC'07. Results**
225 **were partitioned into broadband albedos based on the UV-Visible (0.3 - 0.7 μm), NIR (0.7 - 5.0 μm),**
226 **and the entire spectrum of solar radiation ([SW] 0.3 - 5.0 μm).**

227

228 Fig. 1 illustrates several 2 km x 2 km subsets based on CAR, MODIS, and Landsat retrievals
229 of SW white-sky albedo (WSA) (Fig. 1a –d), broadband NDVI (Fig. 1e –h), as well as a true-color
230 IKONOS scene retrieved on 1 July 2007 (Fig. 1i). The red circle over the IKONOS scene denotes
231 the ~960 m ground diameter footprint as seen by the downward-facing pyranometer atop the
232 CART site's 60 m radiation tower. Throughout the analysis stage in Section 4, a Gaussian filter
233 was applied to the CAR, MODIS, and Landsat data to compute spatially-integrated albedos that
234 represented the tower's ground-projected instantaneous field of view (GIFOV) (Fig. 1j).

235 In order to quantify the temporal consistency of albedo retrievals during the period of
236 CLASIC'07, estimates of broadband NDVI were generated for each sensor (e.g. Fig. 1e – h).
237 NDVI estimates based on broadband white-sky albedos were used to minimize the influence of
238 variable sun-target-sensor configurations when estimating measurement differences and changes
239 in vegetation conditions (Huete et al. 2002). Results in Fig. 1 show how areas north of the CART
240 site and the winter wheat fields just east and west of the site, appear to be more vegetated during
241 the Landsat overpass period (DOY 154). However, the overall change in NDVI was relatively
242 small throughout the CLASIC'07 period (DOY 153-190) (i.e., ~5.7% for the entire study area
243 and ~8.0% for the area within the CART tower footprint).

244 The WSA results in Fig. 1a – 1d show some similarities between the CAR-CRM and MOD-
245 IS WSA data, as well as some differences between the finer resolution Landsat and CAR-MRM
246 albedos. In particular, the Landsat albedos (Fig. 1a) could resolve fine-scale spatial features
247 across the CART site (e.g., small buildings and dirt roads); but were also characterized by higher
248 ‘within-biome’ variability. This is demonstrated in Fig. 2, which illustrates the overall mean and
249 standard deviations in white-sky albedo based on individual estimates obtained for each repre-
250 sentative land cover class identified across the CART site. The ancillary land cover data is based
251 on field surveys, vegetation measurements, and surface characterizations performed during
252 CLASIC'07 (Román et al. 2011a). Unlike the MODIS and CAR intrinsic albedos, which are dri-
253 ven by the anisotropy of each pixel, the Landsat retrieval scheme is based on per-class MODIS
254 BRDF shapes based on uniform land cover characteristics. This resulted in WSA retrievals of
255 varying magnitudes, particularly across mixed cover types (e.g., bare soil mixed with short

256 grass). This is in contrast to the relatively lower within-biome variability seen in the CAR and
257 MODIS white-sky albedos across all land cover classes and broadband channels.

258 Additional quality assurance (QA) checks were performed to assess the consistency of each
259 retrieval scheme. For this study, both the Landsat and MODIS intrinsic albedos were based on
260 gap-free, quality-enhanced BRDF retrievals that rely on spatial and temporal fitting techniques to
261 compensate for missing data and provide an estimate of the surface reflectance anisotropy for
262 situations under cloud-contaminated conditions (Zhang 2008). For the period surrounding the
263 Landsat date of acquisition, the MODIS retrievals were all based on high-quality “majority” full
264 inversion values. Conversely, the data acquisition period surrounding the CAR measurements
265 (DOY 175) was impacted by changing weather conditions (e.g., clouds and rainfall events).
266 These weather conditions resulted in the majority of MODIS retrievals to be based on lower-
267 quality temporally-fitted pixels; particularly, throughout DOY 161-190. Consequently, MODIS
268 retrievals provided a close, but not exact, representation of the surface conditions surrounding
269 the CAR measurements during the CLASIC’07 experiment. For an in-depth look at the MODIS
270 and CAR quality assurance assessment, readers are referred to Section 3 in Román et al.,
271 (2011a), where QA summaries based on data from CLASIC Flight #1928 are available.

272 Understanding the above mentioned differences in BRDF/albedo retrieval strategies and data
273 acquisition periods, it is important to note that the ground-based observations obtained at the
274 CART site provide a consistent reference source for all albedo reconstructions (albeit for a small
275 area the size of a few MODIS pixels) (*cf.*, Section 4). Furthermore, as we will demonstrate in

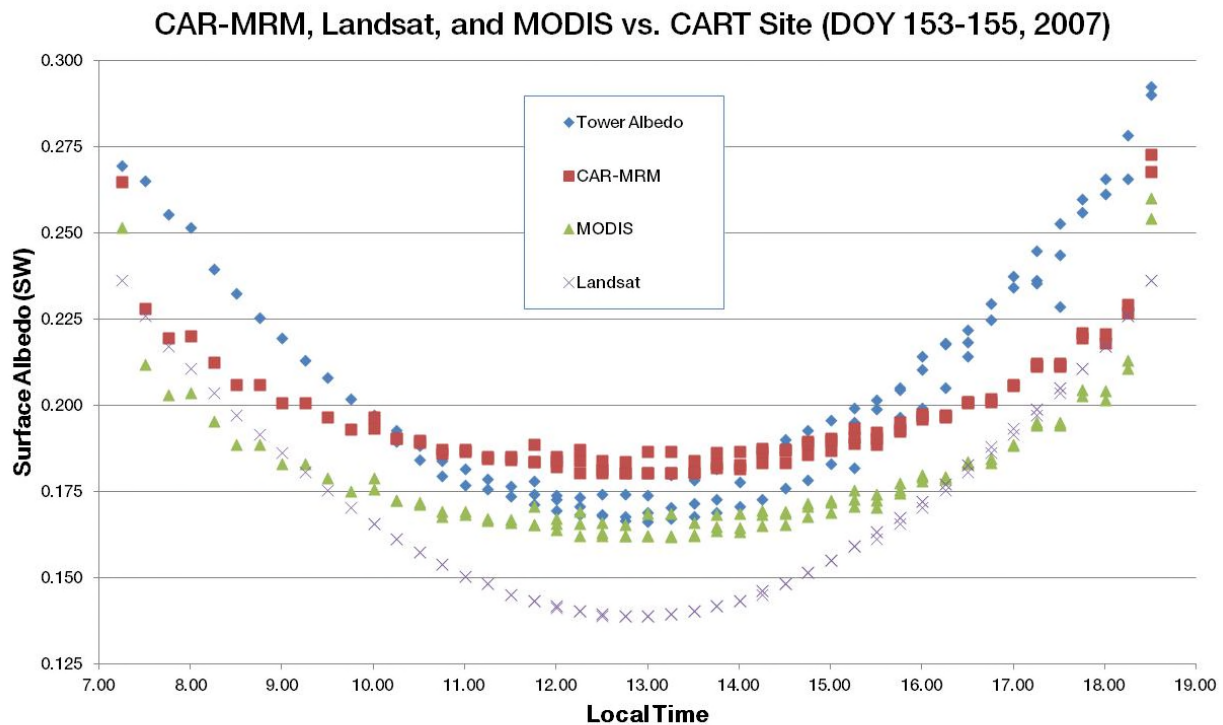
276 Section 5, the CAR data can help reduce the propagation of measurement uncertainty and error
277 when evaluating the satellite-based retrieval schemes at the individual pixel level.

278 **4. Comparisons to tower-based measurements**

279 We now examine the diurnal performance of instantaneous albedos derived from CAR,
280 MODIS, and Landsat, based on comparisons against available in situ observations acquired dur-
281 ing CLASIC'07. Measurements from a downward-facing pyranometer installed on a 60 m radia-
282 tion tower at the CART site collected albedo and radiation fluxes in the shortwave (SW) (0.3- 2.8
283 μm) waveband (Fig.1i). Two additional instruments, a normal incidence pyrheliometer mounted
284 on an automatic sun tracker and a shaded pyranometer riding on top of the sun tracker, measured
285 direct and diffuse solar radiation incident upon the field station (*cf.*, Fig. 3 in Román et al.,
286 2011a). Estimates of cloud fraction and aerosol optical depth, as viewed from a skyward-looking
287 pyranometer and an AERONET sunphotometer (Holben et al. 2001), were also collected. This
288 measurement scheme follows a strict set of guidelines as established by the International Base-
289 line Surface Radiation Network (BSRN) (McArthur 2005; WMO 2006). BSRN measurement
290 protocols are recognized as the international standard for in situ albedo data, with a review
291 process that includes additional quality assurance (QA) checks (e.g. standard units, naming con-
292 ventions, and reporting intervals) to maintain consistency within the larger network-wide BSRN
293 database (Schaaf et al. 2009).

294 Following the albedo reconstruction periods described in Table 1, results in Figs. 3 and 4
295 show comparisons between the tower-based albedos and instantaneous albedos derived from
296 CAR, MODIS, and Landsat data. Measurements of aerosol optical depth (AOD) at 550 nm are

297 also plotted in Fig. 4 (right-axis); while AOD measurements recorded during DOY 153-155 (Fig.
298 3) remained low and constant throughout this period (i.e., $AOD = 0.1676 \pm 0.0590$). Results
299 show the usual “U-shaped” diurnal trend in instantaneous albedo that reaches a minimum value
300 around local solar noon time. In general, the CAR and MODIS albedos met the absolute accura-
301 cy requirement of 0.02 units (i.e., within 10% of surface measured values) for instantaneous SW
302 albedos at $SZA < 45^\circ$ (i.e., between 10.00 and 16.00 local time); with the CAR-CRM albedo data
303 also performing well at $SZA > 45^\circ$ (i.e., before 10.00 and after 16.00 local time). Conversely,
304 both MODIS and Landsat consistently underestimated the tower albedos at $SZA > 45^\circ$. The sta-
305 tistical results in Tables 2 and 3 show similar negative trends in the biases derived from MODIS
306 and Landsat albedos. Finally, CAR and MODIS retrievals based on the full expression of instan-
307 taneous albedo (Eq. 6) showed slight improvements by ~0.0065 absolute units over the isotropic
308 albedo formulation (Eq. 5). As seen for several dates in Fig. 4, the full expression results for
309 MODIS and CAR are much closer to the daily albedo maxima at $SZA = 75^\circ$.



310
 311 **Fig. 3.** Comparisons between instantaneous retrievals of surface albedo (15-min intervals) derived
 312 from CAR-MRM (red squares), MODIS (green triangles), Landsat ('X' marks), and tower-based
 313 measurements (blue diamonds) acquired at the CART site throughout a 3-day period surrounding
 314 the Landsat overpass date (DOY 154, 2007).

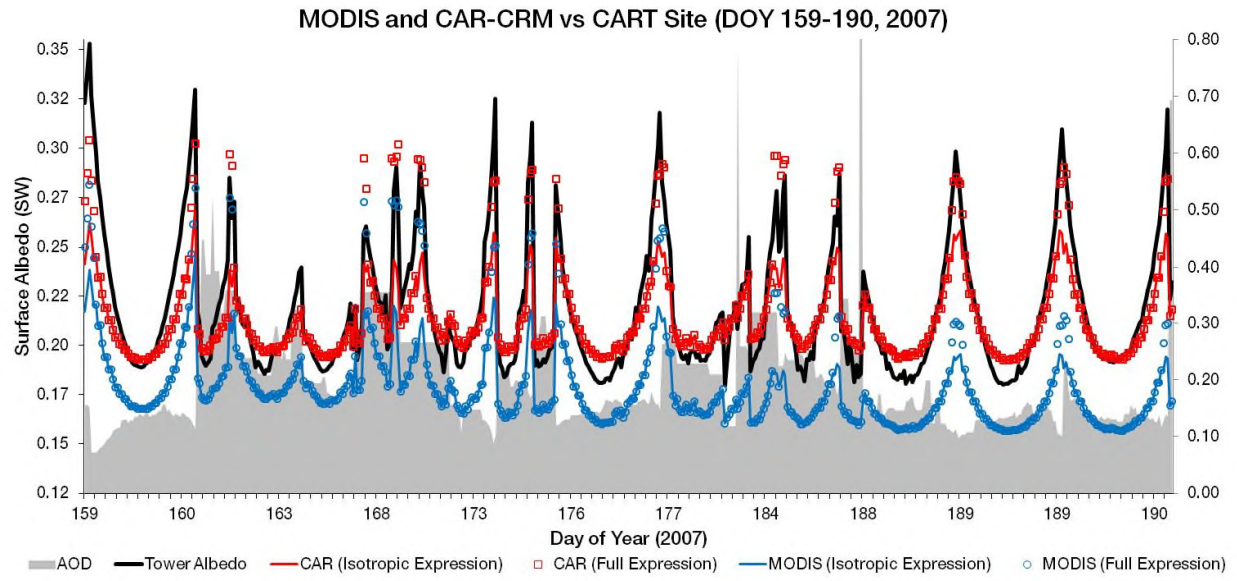
315 **Table 2.** Accuracy^a, (absolute bias) and uncertainty^b (RMS of absolute error or RMSE) values re-
 316 sulting from comparisons between ground-based (CART), airborne (CAR-MRM), and sa-
 317 tellite-derived (MODIS and Landsat) albedos as illustrated in Fig. 3. The total sample size (n) for
 318 two solar zenith angle (SZA) ranges is shown.

| DOY 153-155,2007 | $10^\circ \leq \text{SZA} \leq 45^\circ$ (n = 69) | | | $45^\circ \leq \text{SZA} \leq 75^\circ$ (n = 34) | | |
|--------------------|---|---------|---------|---|---------|---------|
| | CAR-MRM | MODIS | Landsat | CAR-CRM | MODIS | Landsat |
| Accuracy (Bias) | 0.0044 | -0.0136 | -0.0324 | -0.0266 | -0.0433 | -0.0401 |
| Uncertainty (RMSE) | 0.0090 | 0.0157 | 0.0327 | 0.0287 | 0.0447 | 0.0407 |

320
 321 ^aAccuracy = arithmetic mean (Sensor – Tower)

322 ^bUncertainty: RMS of absolute error = $\sqrt{\text{arithmetic mean} (\text{Sensor} - \text{Tower})^2}$

323



324
 325 **Fig. 4. Comparisons between instantaneous albedos (30-min intervals) derived from CAR-CRM**
 326 **and MODIS (using both isotropic and full expressions), and tower-based measurements acquired at**
 327 **the CART site throughout a 32-day period surrounding CLASIC Flight #1928 (DOY 175, 2007).**

328
 329
 330 **Table 3. Accuracy and uncertainty values resulting from a 32-day comparison between ground-**
 331 **based (CART), airborne (CAR-CRM), and satellite-derived (MODIS) albedos as illustrated in Fig.**
 332 **4. Setup is the same as Table 2.**

| DOY 159-190,2007 | $10^\circ \leq \text{SZA} \leq 45^\circ$ (n = 289) | | $45^\circ \leq \text{SZA} \leq 75^\circ$ (n = 193) | |
|--------------------|--|---------|--|---------|
| | CAR-CRM | MODIS | CAR-CRM | MODIS |
| Accuracy (Bias) | 0.0042 | -0.0286 | -0.0096 | -0.0495 |
| Uncertainty (RMSE) | 0.0082 | 0.0296 | 0.0184 | 0.0526 |

333 5. Regional assessment of MODIS and Landsat albedos

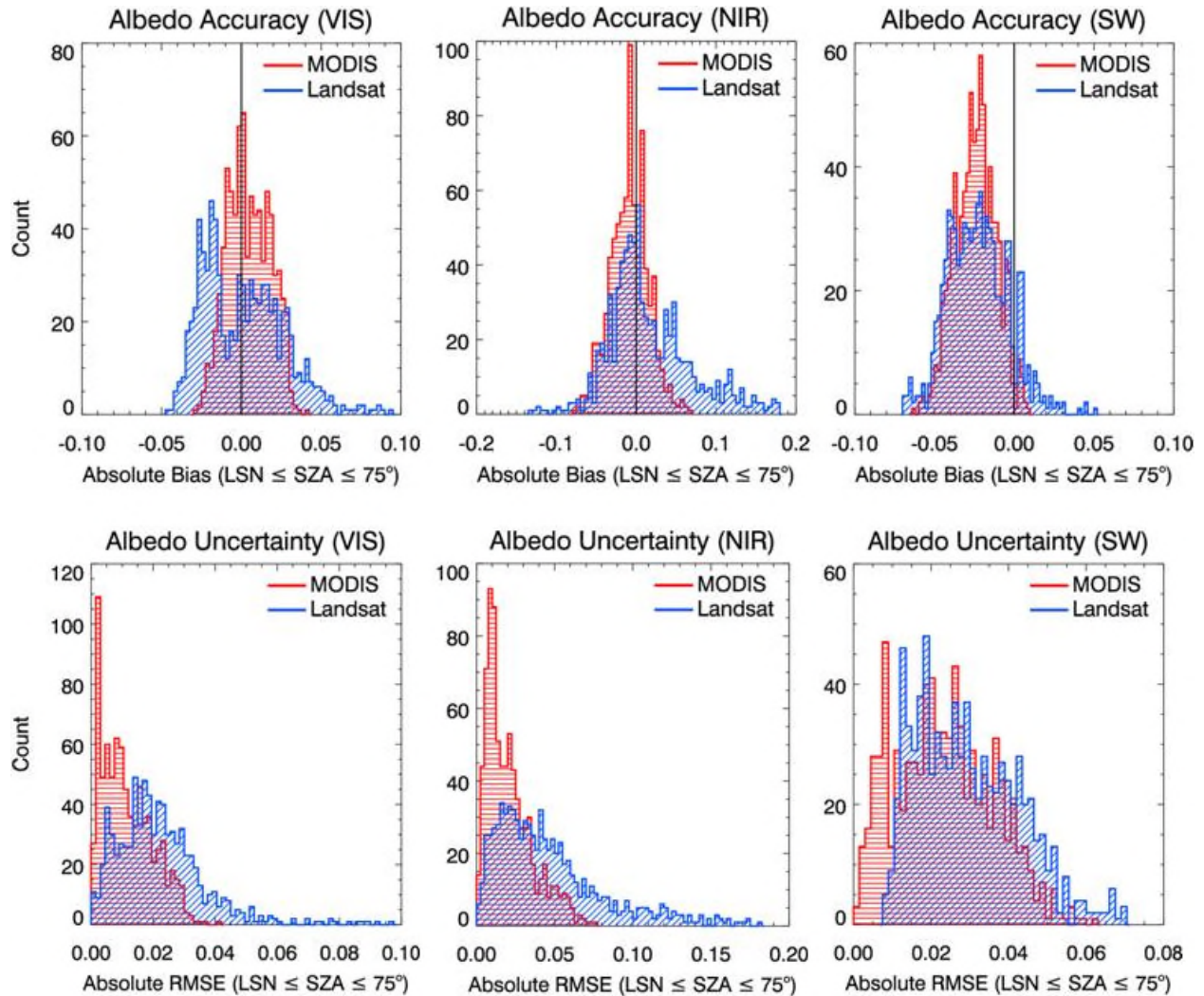
334 In the previous section, CAR retrievals were shown to be of sufficient accuracy and consistency to reproduce the diurnal variations in albedo across the CART site throughout the entire period of CLASIC'07. Using the CAR-MRM and CAR-CRM instantaneous albedos as "ground-truth", we now employ standard error propagation techniques (Heuvelink 1998) to quantify the uncertainties associated with MODIS and Landsat instantaneous albedos over a mixture of landscapes extending beyond the tower observation footprint at the CART site.

341 Assuming that the error propagation terms in Eqs. (14 -15) are uncorrelated, the Root-Sum-
342 of-Squares Error (RSSE) can be used to provide estimates of retrieval uncertainty (absolute
343 RMSE) and bias, both in an absolute and temporal sense:

344
$$RSSE_{MODIS} = \sqrt{Err(\hat{\theta}_{tower \rightarrow CAR-CRM})^2 + Err(\hat{\theta}_{CAR-CRM \rightarrow MODIS})^2} \quad (14)$$

345
$$RSSE_{Landsat} = \sqrt{Err(\hat{\theta}_{tower \rightarrow CAR-MRM})^2 + Err(\hat{\theta}_{CAR-MRM \rightarrow Landsat})^2} \quad (15)$$

346 where $Err(\hat{\theta}_x)$ denotes the “in-situ to satellite” error propagation chain based on two component
347 factors. CAR BRDF/albedo retrievals were then matched to the resolution of MODIS and Land-
348 sat to minimize errors due to sub-grid scale mismatch and the effects of land surface heterogenei-
349 ty. Additional checks were also performed to limit the sampling of CAR pixels to the highest
350 quality “majority” full BRDF inversion values. For CLASIC’07, this resulted in 789 individual
351 samples, each of which was tested following the same albedo reconstruction periods presented in
352 Section 3.



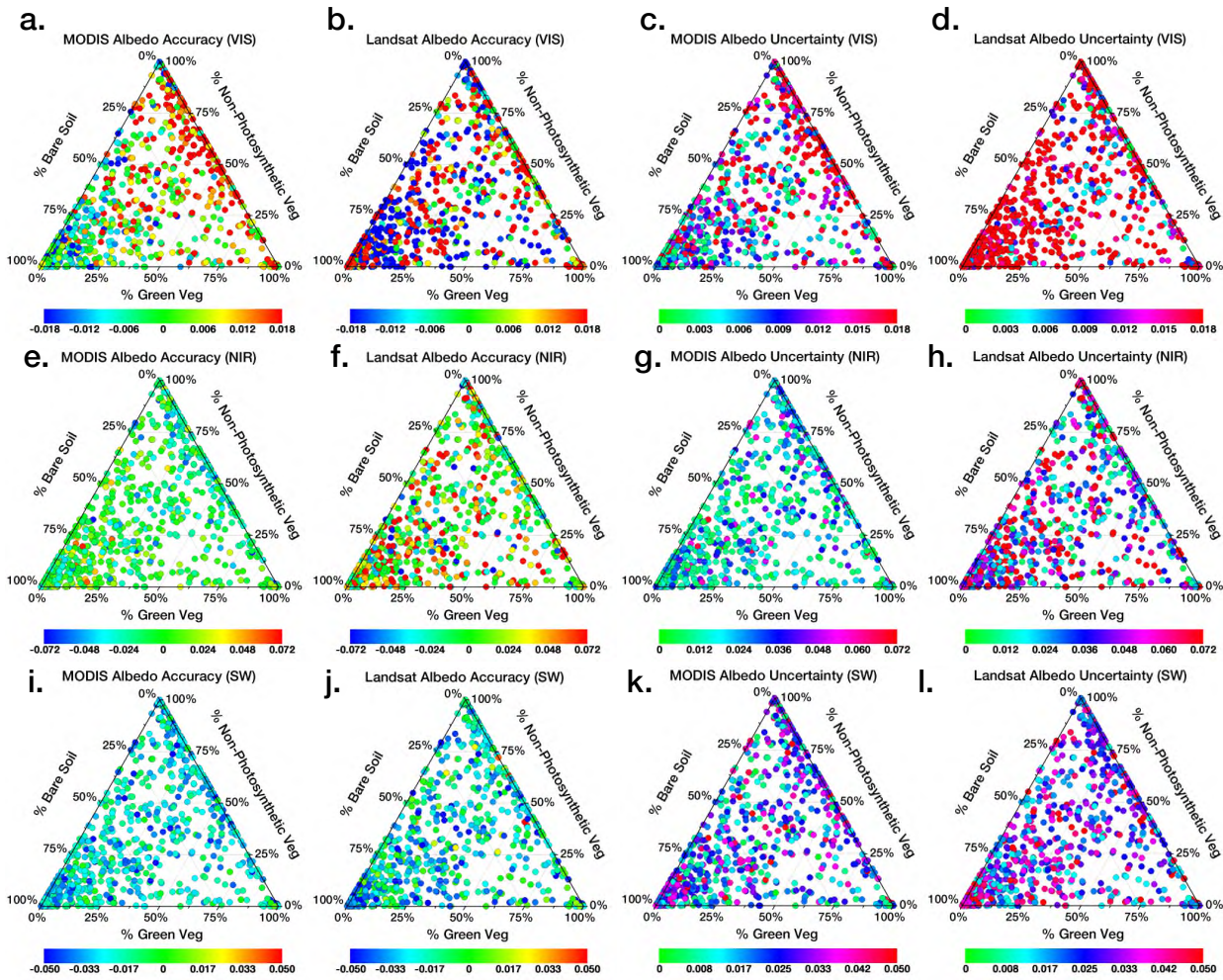
353
354 **Fig. 5. Distribution of absolute bias (accuracy) and RMSE (uncertainty) for MODIS and Landsat**
355 **instantaneous albedos at UV-Visible, NIR, and SW broadband channels for the CLASIC'07 period**
356 **over the CART site.**

357 Results were examined by comparing the distribution of biases and RMSEs resulting from
358 MODIS and Landsat instantaneous albedos at $LSN \leq SZA \leq 75^\circ$. The histogram plots in Fig. 5
359 show a persistent negative bias (-0.03) in SW instantaneous albedos, corresponding to the biases
360 recorded for MODIS and Landsat in earlier assessments (*cf.*, results in Tables 2 and 3). Likewise,
361 for the NIR broadband, roughly 19% of Landsat retrievals showed positive biases above the
362 standard accuracy limit of ± 0.072 units. In the VIS broadband, a small fraction of MODIS (23%)

363 and a large fraction of Landsat retrievals (57%) were also above the standard accuracy limit of
364 ± 0.018 units. To understand the causes of such differences, a collection of ternary diagrams were
365 created to determine how each sensor performed at the individual pixel level. The diagrams in
366 Fig. 6 have been arranged such that retrievals located near the top originate from landscapes
367 dominated by non-photosynthetic (or 'brown') vegetation (i.e., combined land cover (LC) classes
368 1, 4, and 5 in Fig. 2). Conversely, retrievals located near the bottom-left correspond to areas
369 dominated by bare soils (i.e., combined LC classes 6, 7, and 8 in Fig. 2), and retrievals located
370 near the bottom-right correspond to areas dominated by green vegetation (i.e., combined LC
371 classes 2, and 3 in Fig. 2). Thus, the closer the satellite retrievals are to the center portions of the
372 ternary diagrams, the more mixed is the landscape.

373 Results reveal a large degree of variability in the RMSE and bias estimates of MODIS and
374 Landsat albedos, both between fractional cover types and across broadband channels. In particu-
375 lar, the MODIS NIR values remained stable across most landscape regimes, with only a few
376 samples identified above the 20% margin of error for snow-free conditions (Fig. 6e). A synoptic
377 analysis of the ternary diagrams also suggests that the uncertainties in the NIR broadband are
378 more likely to propagate into the SW domain (Figs. 6i –6l). The MODIS VIS broadband also ap-
379 peared to capture bare-soil albedo variability (i.e., wet vs. dry areas) with high accuracy (-0.008);
380 but the biases were moderately larger over mixed landscapes (+0.012) and regions dominated
381 by non-photosynthetic vegetation (+0.019) (Fig. 6a). Conversely, the Landsat albedos were less
382 stable in the NIR, with positive biases (+0.05) dominating over mixed landscapes (Fig. 6f). The
383 same error patterns were seen in the VIS broadband, where more than half of Landsat retrievals

384 were above the 20% margin of error (Fig. 6d). The latter resulted from varying magnitudes
 385 across mixed cover types and regions dominated by bare soils (Fig. 6b).



386
 387 **Fig. 6. Ternary diagrams illustrating the pixel-specific accuracy (absolute bias)
 388 and uncertainty (absolute RMSE) of MODIS and Landsat instantaneous albedos (LSN \leq SZA \leq 75) at UV-Visible (a.
 389 – d.), NIR (e. – d.), and SW (i. – l.) broadband channels for the CLASIC'07 period over the CART
 390 site. For each color scale, green denotes values where the bias or RMSE = 0. For the accuracy dia-
 391 grams, the lower (blue) and upper (red) limits correspond to retrievals that are at or above a 20%
 392 margin of error (i.e., relative to in-situ measurements obtained under snow-free conditions). For the
 393 uncertainty diagrams, the upper (red) limit denotes the same (20%) margin of error.**
 394

395 For the period of CLASIC'07, there were two major factors that contributed to the uncer-
 396 tainties in the satellite-derived albedo values. First, it is unlikely that the assumption of temporal

397 stability in the retrieval of 500 m MODIS BRDFs could hold together throughout the extended
398 periods of cloud-contaminated observations experienced during CLASIC'07. Daily records from
399 land cover surveys performed on DOY 166-173 over landscapes surrounding the CART site con-
400 firm that several parcels of corn, milo, and winter-wheat were being harvested before full maturi-
401 ty due to floods experienced along the Salt Fork Arkansas River (located 5 km north of the
402 CART site). A visual inspection of the 2.4 m IKONOS scene acquired on 1 July (Fig. 1i) also
403 confirms these events. Thus, it is likely that the negative (-0.03) biases in MODIS SW albedos
404 are caused by the use of temporally-fitted BRDF shapes that are driven by “majority” full inver-
405 sion values obtained prior to the early harvesting period (i.e., DOY 145-153, 2007). This may
406 explain why the uncertainties of MODIS VIS albedos where predominantly above the 20% mar-
407 gin of error over areas dominated by senescent winter-wheat fields; but remained well under the
408 10% margin of error over areas dominated by bare soils.

409 For the Landsat albedos, another major source of uncertainty is the assumption of spatial and
410 structural uniformity at the Landsat (30 m) pixel scale. In the Landsat albedo retrieval algorithm,
411 “pure” land cover clusters are identified on a regional basis and then associated with MODIS
412 anisotropy information through scaling of 500 m BRDF retrievals to 30 m resolution. However,
413 recent assessments of the CLASIC Flight #1928 dataset have indicated that the use of dominant
414 archetypal BRDF shapes to describe the anisotropy of heterogeneous pixels may lead to errors on
415 the order of 0.5% – 6.5% in the retrieved directional reflectance values (*cf.*, Fig.10 in Román et
416 al., 2011a). This will particularly affect retrievals where heterogeneous conditions are being
417 lumped into a single land cover class (e.g., bare soil areas not being properly partitioned into dry,
418 wet, and damp conditions.) As discussed in Shuai et al., (2011) these situations can be addressed

419 by breaking “pure” land cover clusters into multiple sub-clusters representing different surface
420 conditions.

421 **6. Conclusions and future recommendations**

422 The diurnal performance of the MODIS and Landsat albedo algorithms (Schaaf et al. 2002;
423 Shuai et al. 2011) is evaluated using field and airborne measurements coincident with Landsat
424 TM and multi-date MODIS Terra/Aqua overpasses. For the broad range of mixed vegetation and
425 structural types examined during the period of CLASIC’07, the overall accuracy of MODIS and
426 Landsat SW (0.3 -5.0 μm) albedos is within a 10% margin of error and shows an increasing neg-
427 ative bias (-0.03) and increased RMSE (0.05) as zenith angle increases compared with the in-situ
428 measurements. Results also reveal a high degree of variability in the RMSE and bias of MODIS
429 and Landsat albedos in both the visible (0.3 - 0.7 μm) and near-infrared (0.7 - 5.0 μm) broadband
430 channels. However, we note that the lack of high-quality “majority” 500m MODIS BRDF pixels
431 through the experiment hindered the band-dependent quality controls, as outliers were more dif-
432 ficult to identify. This was particularly the case in the VIS broadband, where cloud contamination
433 and mixed-pixel contamination are highly likely. Despite such limitations, results obtained indi-
434 cate that MODIS VIS/NIR albedos are able to capture bare-soil albedo variability (i.e., wet vs.
435 dry areas) with high accuracy (-0.008).

436 While recent product development, intercomparison, and validation efforts have focused al-
437 most entirely on the retrieval of surface albedos for a single SW broadband value, it is important
438 to note that most numerical prediction models (and global climate and biogeochemical models)
439 currently in use call for surface energy fluxes and some biophysical variables to be calculated

440 separately by disentangling broadband albedos into fractional areas of bare soil and vegetation
441 (Noilhan and Mahfouf 1996; Koster et al. 2000; Ek et al. 2003; Kaptué et al. 2010). It is there-
442 fore important to continue examining how the accuracies of global albedo products are holding
443 up in these spectral regimes. Likewise, the uncertainties that may impact satellite-inferred albedo
444 trends must be assessed and expressed in terms of a reference sensor that can overcome the fore-
445 told errors due to sub-grid scale mismatch and the effects of land surface heterogeneity. It is thus
446 critical that continuous, long-term tower measurements of surface albedo and radiation fluxes be
447 done in concert with intensive airborne measurement campaigns that can focus on addressing
448 sources of uncertainties at both plot-level (< 90 m) to landscape-level (> 90 m) scales.

449 It is clear that spatial scale of signal aggregation is very important in the retrieval of mea-
450 ningful surface radiation properties of vegetated surfaces from multiangle and pseudo-multi-
451 angular remote sensing data. This is forcing experimenters to develop new measurement and va-
452 lidation protocols for surface BRDF and albedo estimation (Walshall et al. 2000; Schaaf et al.
453 2009). Ongoing studies combining airborne multiangular measurements from CAR with mea-
454 surements of terrestrial biomass and ecosystem structure, e.g., NASA's L-band Digital Beam-
455 forming Synthetic Aperture Radar (DBSAR) (Rincon et al. 2011) and the Slope Imaging Multi-
456 polarization Photon-counting Lidar (SIMPL) (Dabney et al. 2010), will provide us with new in-
457 sights to issues of landscape-level variability and the opportunity to continue examining mixed
458 pixels from both medium and coarse scale resolution systems.

459 **Bibliography**

- 460 Augustine, J.A., Hodges, G.B., Cornwall, C.R., Michalsky, J.J., & Medina, C.I. (2005). An up-
461 date on SURFRAD - The GCOS surface radiation budget network for the continental United
462 States. *Journal of Atmospheric and Oceanic Technology*, 22, 1460-1472.
- 463 Barnes, C.A., & Roy, D.P. (2008). Radiative forcing over the conterminous United States due to
464 contemporary land cover land use albedo change. *Geophysical Research Letters*, 35, L09706.
465 doi:10.1029/2008GL033567.
- 466 Berk, A., Cooley, T.W., Anderson, G.P., Acharya, P.K., Bernstein, L.S., Muratov, L., Lee, J.,
467 Fox, M.J., Adler-Golden, S.M., Chetwynd, J.H., Hoke, M.L., Lockwood, R.B., Gardner, J.A., &
468 Lewis, P.E. (2004). MODTRAN5: A Reformulated Atmospheric Band Model with Auxiliary
469 Species and Practical Multiple Scattering Options, Sensors, Systems, and Next-Generation Satel-
470 lites. *VIII. Proceedings of the Society of Photographic Instrumentation Engineers (SPIE)*, 5571,
471 78-85
- 472 Bindlish, R., Jackson, T., Sun, R., Cosh, M., Yueh, S., & Dinardo, S. (2009). Combined passive
473 and active microwave observations of soil moisture during CLASIC. *IEEE Geoscience and Re-*
474 *lcome Sensing Letters*, 6, 644-648. doi:10.1109/LGRS.2009.2028441.
- 475 Butler, J.J., & Barnes, C.A. (2003). The use of transfer radiometers in validating the visible to
476 shortwave infrared calibrations of radiance sources used by instruments in NASA's Earth Ob-
477 serving System. *Metrologia*, 40, S70-S77. doi:10.1088/0026-1394/40/1/316.
- 478 Dabney, P., Harding, D., Abshire, J., Huss, T., Jodor, G., Machan, R., Marzouk, J., Rush, K.,
479 Seas, A., Shuman, C., Sun, X., Valett, S., Vasilyev, A., Yu, A., & Zheng, Y. (2010). The Slope
480 Imaging Multi-polarization Photon-counting Lidar: Development and performance results *Pro-*
481 *ceedings of the Geoscience and Remote Sensing Symposium (IGARSS'10), Honolulu, HI*, 653 -
482 656. doi:10.1109/IGARSS.2010.5650862
- 483 Ek, M.B., Mitchell, K.E., Lin, Y., Rogers, E., Grunmann, P., Koren, V., Gayno, G., & Tarpley,
484 J.D. (2003). Implementation of the upgraded Noah land surface model in the National Centers
485 for Environmental Prediction operational mesoscale Eta model. *Journal of Geophysical Re-*
486 *search*, 108 (D22), 8851. doi:10.1029/2002JD003296.
- 487 Gao, F., Masek, J., Schwaller, M., & Hall, F. (2006). On the blending of the Landsat and MODIS
488 surface reflectance: Predicting daily Landsat surface reflectance. *IEEE Transactions on Geos-*
489 *cience and Remote Sensing*, 44, 2207-2218. doi:10.1109/TGRS.2006.872081.
- 490 Gatebe, C.K., Butler, J.J., Cooper, J.W., Kowalewski, M., & King, M.D. (2007). Characteriza-
491 tion of errors in the use of integrating-sphere systems in the calibration of scanning radiometers.
492 *Applied Optics*, 46, 7640-7651.
- 493 Gatebe, C.K., King, M.D., Platnick, S., Arnold, G.T., Vermote, E.F., & Schmid, B. (2003). Air-
494 borne spectral measurements of surface-atmosphere anisotropy for several surfaces and ecosys-
495 tems over southern Africa. *Journal of Geophysical Research*, 108(D13).
496 doi:10.1029/2002JD002397.

- 497 Heathman, G.C., Larose, M., Cosh, M.H., & Bindlish, R. (2009). Surface and profile soil mois-
498 ture spatio-temporal analysis during an excessive rainfall period in the Southern Great Plains,
499 USA. *CATENA*, 78, 159-169. doi:10.1016/j.catena.2009.04.002.
- 500 Heuvelink, G.B.M. (1998). *Error propagation in environmental modeling with GIS*.
- 501 Holben, B.N., Tanre, D., Smirnov, A., Eck, T.F., Slutsker, I., N., A., Newcomb, W.W., Schafer,
502 J., Chatenet, B., Lavenue, F., Kaufman, Y.J., J., V.-C., Setzer, A., Markham, B., Clark, D.,
503 Frouin, R., Halthore, R., Karnieli, A., O'Neill, N.T., Pietras, C., Pinker, R.T., Voss, K., & Zibordi,
504 G. (2001). An emerging ground-based aerosol climatology: Aerosol Optical Depth from
505 AERONET. *Journal of Geophysical Research*, 106, 12067-12097.
- 506 Huete, A., Didan, K., Miura, T., Rodriguez, E.P., Gao, X., & Ferreira, L.G. (2002). Overview of
507 the radiometric and biophysical performance of the MODIS vegetation indices. *Remote Sensing*
508 of Environment, 83, 195-213. doi:10.1016/S0034-4257(02)00096-2.
- 509 Jin, Y.F., Schaaf, C.B., Gao, F., Li, X.W., Strahler, A.H., Lucht, W., & Liang, S.L. (2003a).
510 Consistency of MODIS surface bidirectional reflectance distribution function and albedo retriev-
511 als: 1. Algorithm performance. *Journal of Geophysical Research*, 108, D5.
512 doi:10.1029/2002JD002803.
- 513 Jin, Y.F., Schaaf, C.B., Woodcock, C.E., Gao, F., Li, X.W., Strahler, A.H., Lucht, W., & Liang,
514 S.L. (2003b). Consistency of MODIS surface bidirectional reflectance distribution function and
515 albedo retrievals: 2. Validation. *Journal of Geophysical Research*, 108, D5.
516 doi:10.1029/2002JD002804.
- 517 Kaptu  , T.A.T., Roujean, J.-L., & Faroux, S. (2010). ECOCLIMAP-II: An ecosystem classifica-
518 tion and land surface parameter database of western Africa at 1 km resolution for the Africa
519 Monsoon Multidisciplinary Analysis (AMMA) project. *Remote Sensing of Environment*, 114,
520 961-976. doi:10.1016/j.rse.2009.12.008.
- 521 King, M.D., Strange, M.G., Leone, P., & Blaine, L.R. (1986). Multiwavelength scanning radi-
522 ometer for airborne measurements of scattered radiation within clouds. *Journal of Atmospheric*
523 *and Oceanic Technology*, 3, 513-522.
- 524 Koster, R.D., Suarez, M.J., Ducharne, A., Stieglitz, M., & Kumar, P. (2000). A catchment-based
525 approach to modeling land surface processes in a general circulation model 1. Model structure.
526 *Journal of Geophysical Research*, 105, 24809-24822. doi:10.1029/2000JD900327.
- 527 Lee, T.F., Nelson, C.S., Dills, P., Riishojaard, L.P., Jones A, Li L., Miller, S., Flynn, L.E., Jed-
528 lovec, G., McCarty, W., Hoffman, C., & McWilliams, G. (2010). NPOESS: Next-Generation
529 Operational Global Earth Observations. *Bull. Am. Met. Soc.*, 91, 727-740.
530 doi:10.1175/2009BAMS2953.1.
- 531 Lewis, P., & Barnsley, M. (1994). Influence of the Sky Radiance Distribution on Various Formu-
532 lations of the Earth Surface Albedo. *Proceedings of the Colloque International Mesures Physi-
533 ques et Signatures en Teledetection*, 707-716
- 534 Li, X.W., & Strahler, A.H. (1992). Geometric-optical bidirectional reflectance modeling of the
535 discrete crown vegetation canopy - Effect of crown shape and mutual shadowing. *IEEE Transac-
536 tions on Geoscience and Remote Sensing*, 30, 276-292. doi:10.1109/36.134078.

- 537 Liang, S. (2001). Narrowband to Broadband Conversion of Land Surface Albedo. I. Algorithms.
538 *Remote Sensing of Environment*, 76, 213-238.
- 539 Liang, S., Shuey, C., Russ, A., Fang, H., Chen, M., Walthall, C., Daughtry, C., & Jr., R.H.
540 (2003). Narrowband to broadband conversions of land surface albedo. II: Validation. *Remote*
541 *Sensing of Environment*, 84, 25-41.
- 542 Liu, J., Schaaf, C.B., Strahler, A.H., Jiao, Z., Shuai, Y., Zhang, Q., Román, M., Augustine, J.A.,
543 & Dutton, E.G. (2009). Validation of Moderate Resolution Imaging Spectroradiometer (MODIS)
544 albedo retrieval algorithm: Dependence of albedo on solar zenith angle. *Journal of Geophysical*
545 *Research-Atmospheres*, 114, D01106. doi:10.1029/2008JD009969.
- 546 Lucht, W., Schaaf, C.B., & Strahler, A.H. (2000). An algorithm for the retrieval of albedo from
547 space using semi-empirical BRDF models. *IEEE Transactions on Geoscience and Remote Sensing*,
548 38, 977-998. doi:10.1109/36.841980.
- 549 Lyapustin, A.I., & Privette, J.L. (1999). A new method of retrieving surface bidirectional reflec-
550 tance from ground measurements: Atmospheric sensitivity study. *Journal of Geophysical Re-*
551 *search*, 104, 6257-6268.
- 552 Martonchik, J., Bruegge, C., & Strahler, A.H. (2000). A Review of Reflectance Nomenclature
553 Used in Remote Sensing. *Remote Sensing Reviews*, 19, 9-20. doi:10.1080/02757250009532407.
- 554 Masek, J., Huang, H., Wolfe, R.E., Cohen, W.B., Hall, F., Kutler, J., & Nelson, P. (2008). North
555 American forest disturbance mapped from a decadal Landsat record. *Remote Sensing of Envi-*
556 *ronment*, 112, 2914-2926. doi:10.1016/j.rse.2008.02.010.
- 557 Masek, J.G., Vermote, E.F., Saleous, N., Wolfe, R.E., Hall, F.G., Huemmrich, F.K., Gao, F.,
558 Kutler, J., & Lim, T.k. (2006). A Landsat surface reflectance data set for North America, 1990-
559 2000. *Geosciences and Remote Sensing Letters*, 3, 68-72.
- 560 McArthur, L.B.J. (2005). Baseline Surface Radiation Network (BSRN) Operations Manual V2.1,
561 WCRP 121, WMO/TD-No. 1274, April 2005,
562 http://www.wmo.ch/pages/prog/wcrp/PG_Reports_WCRPSeries.html. In: World Climate Re-
563 search Program.
- 564 Morisette, J.T., Privette, J.L., & Justice, C.O. (2002). A framework for the validation of MODIS
565 land products. *Remote Sensing of Environment*, 83, 77-96. doi:10.1016/S0034-4257(02)00088-3.
- 566 Noilhan, J., & Mahfouf, J.-F. (1996). The ISBA land surface parametrisation scheme. *Global*
567 *and Planetary Change*, 13, 145-159. doi:10.1016/0921-8181(95)00043-7.
- 568 Rincon, R.F., Vega, M.A., Buenfil, M., Geist, A., Hilliard, L., & Racette, P. (2011). NASA's L-
569 Band Digital Beamforming Synthetic Aperture Radar *IEEE Transactions on Geoscience and*
570 *Remote Sensing*, 49, 3622-3628. doi:10.1109/TGRS.2011.2157971.
- 571 Román, M.O., Gatebe, C.K., Poudyal, R., Schaaf, C.B., Wang, Z., & King, M.D. (2011a). Varia-
572 bility in surface BRDF at different spatial scales (30 m-500 m) over a mixed agricultural land-
573 scape as retrieved from airborne and satellite spectral measurements. *Remote Sensing of Envi-*
574 *ronment*, 115, 2184-2203. doi:10.1016/j.rse.2011.04.012

- 575 Román, M.O., Justice, C., Csiszar, I., Key, J.R., Devadiga, S., Davidson, C., Wolfe, R., & Pri-
576 vette, J. (2011b). Pre-launch evaluation of the NPP VIIRS Land and Cryosphere EDRs to meet
577 NASA's science requirements. *Proceedings of the Geoscience and Remote Sensing Symposium*
578 (*IGARSS'11*, Vancouver, BC, 154-157. doi:10.1109/IGARSS.2011.6048921.
- 579 Román, M.O., Schaaf, C.B., Lewis, P., Gao, F., Anderson, G.P., Privette, J.L., Strahler, A.H.,
580 Woodcock, C.E., & Barnsley, M. (2010). Assessing the coupling between surface albedo derived
581 from MODIS and the fraction of diffuse skylight over spatially-characterized landscapes. *Remote*
582 *Sensing of Environment*, 114, 738-760. doi:10.1016/j.rse.2009.11.014.
- 583 Román, M.O., Schaaf, C.B., Yang, X., Woodcock, C.E., Strahler, A.H., Braswell, R.H., Curtis,
584 P.S., Davis, K.J., D., D., Gu, L., Goulden, M.L., Hollinger, D.Y., Kolb, T.E., Meyers, T.P.,
585 Munger, J.W., Privette, J.L., Richardson, A.D., Wilson, T.B., & Wofsy, S.C. (2009). The MOD-
586 IS (Collection V005) BRDF/albedo product: Assessment of spatial representativeness over fo-
587 rested landscapes. *Remote Sensing of Environment*, 113, 2476-2498.
588 doi:10.1016/j.rse.2009.07.009.
- 589 Ross, J. (1981). *The Radiation Regime and Architecture of Plant Stands*. Norwell, Mass.: The
590 Hague: Dr. W. Junk Publishers. ISBN 906193-607-1.
- 591 Roy, D.P., Ju, J., Lewis, P., Schaaf, C.B., Gao, F., Hansen, M., & Lindquist, E. (2008). Multi-
592 temporal MODIS–Landsat data fusion for relative radiometric normalization, gap filling, and
593 prediction of Landsat data. *Remote Sensing of Environment*, 112, 3112-3130.
594 doi:10.1016/j.rse.2008.03.009.
- 595 Salomon, J.G., Schaaf, C.B., Strahler, A.H., Gao, F., & Jin, Y.F. (2006). Validation of the MOD-
596 IS bidirectional reflectance distribution function and albedo retrievals using combined observa-
597 tions from the Aqua and Terra platforms. *IEEE Transactions on Geoscience and Remote Sens-*
598 *ing*, 44, 1555-1565. doi:10.1109/TGRS.2006.871564.
- 599 Schaaf, C.B., Cihlar, J., Belward, A., Dutton, E., & Verstraete, M. (2009). *Albedo and Reflec-*
600 *tance Anisotropy, ECV-T8: Assessment of the status of the development of standards for the Ter-*
601 *restrial Essential Climate Variables*. Rome: FAO.
- 602 Schaaf, C.B., Gao, F., Strahler, A.H., Lucht, W., Li, X., Tsang, T., Strugnell, N.C., Zhang, X.,
603 Jin, Y., Muller, J.-P., Lewis, P., Barnsley, M., Hobson, P., Disney, M., Roberts, G., Dunderdale,
604 M., Doll, C., d'Entremont, R., Hu, B., Liang, S., Privette, J.L., & Roy, D.P. (2002). First opera-
605 tional BRDF, albedo and nadir reflectance products from MODIS. *Remote Sensing of Environ-*
606 *ment*, 83, 135-148. doi:10.1016/S0034-4257(02)00091-3.
- 607 Schaepman-Strub, G., Schaepman, M.E., Painter, T.H., Dangel, S., & Martonchik, J.V. (2006).
608 Reflectance quantities in optical remote sensing-definitions and case studies. *Remote Sensing of*
609 *Environment*, 103, 27-42. doi:10.1016/j.rse.2006.03.002.
- 610 Shuai, Y., Masek, J., Gao, F., & C.B., S. (2011). An Algorithm for the Retrieval of 30m snow-
611 free albedo from Landsat surface reflectance and MODIS BRDF. *Remote Sensing of Environ-*
612 *ment, submitted*, 115, 2204-2216. doi:10.1016/j.rse.2011.04.019.

- 613 Susaki, J., Yasuoka, Y., Kajiwara, K., Honda, Y., & Hara, K. (2007). Validation of MODIS al-
614 bedo products of paddy fields in Japan. *IEEE Transactions on Geoscience and Remote Sensing*,
615 45, 206-217. doi:10.1109/TGRS.2006.882266.
- 616 Trishenko, A., Luo, Y., Cribb, M., & Hamm, K. (2003). Surface Spectral Albedo Intensive Op-
617 erational Period at the ARM SGP Site in August 2002: Results, Analysis, and Future Plans. In:
618 [<http://iop.archive.arm.gov/arm-iop/2002/sgp/sfcalb/>] ARM Intensive Operational Period (IOP)
619 Data Browser.
- 620 Walthall, C., Roujean, J.-L., & Morisette, J. (2000). Field and landscape BRDF optical wave-
621 length measurements: Experience, techniques and the future. *Remote Sensing Reviews*, 18, 503-
622 531. doi:10.1080/02757250009532399.
- 623 Wang, Z., Schaaf, C.B., Strahler, A.H., Wang, J., Woodcock, C.E., Chopping, M.J., Román,
624 M.O., Rocha, A.V., & Shuai, Y. (2011). Evaluation of Moderate-resolution Imaging Spectrora-
625 diometer (MODIS) snow albedo product (MCD43A) over tundra. *Remote Sensing of Environ-
626 ment*. doi:10.1016/j.rse.2011.10.002.
- 627 Wanner, W., Li, X., & Strahler, A.H. (1995). On the Derivation of Kernels for Kernel-Driven
628 Models of Bidirectional Reflectance. *Journal of Geophysical Research*, 100, 21077-21089.
629 doi:10.1029/95JD02371.
- 630 Wanner, W., Strahler, A.H., Hu, B., Lewis, P., Muller, J., Li, X., Schaaf, C.B., & Barnsley, M.
631 (1997). Global retrieval of bidirectional reflectance and albedo over land from EOS MODIS and
632 MISR data: Theory and algorithm. *Journal of Geophysical Research*, 102, 17143-17161.
633 doi:10.1029/96JD03295.
- 634 WMO (2006). World Meteorological Organization Commission for Instruments and Methods of
635 Observation (WMO/CIMO) Guide to Meteorological Instruments and Methods of Observation.
636 Preliminary seventh edition. Report WMO-No. 8, Geneva, Switzerland.
637 <http://www.wmo.int/pages/prog/www/IMOP/publications/CIMO-Guide/Draft-7-edition.html>:
638 <http://www.wmo.ch/pages/prog/www/IMOP/publications/WMO-8-Guide-contents.html>.
- 639 Zhang, Q. (2008). A Global Spatially and Temporally Complete Reflectance Anisotropy Data-
640 base to Improve Surface Characterization for Albedo Modeling. In, *PhD Thesis, Department of
641 Geography and Environment* (p. 155). Boston, MA: Boston University.
- 642
- 643